Journal of Alloys and Compounds 509 (2011) 4160–4166

Contents lists available at ScienceDirect

Journal of Alloys and Compounds

journal homepage: www.elsevier.com/locate/jallcom

Synthesis and conductivity of $GdPO_4$ nanorods: Impacts of particle size and Ca^{2+} doping

Heng Wang, Guangshe Li, Xiangfeng Guan, Liping Li*

Key Laboratory of Optoelectronic Materials Chemistry and Physics, Fujian Institute of Research on the Structure of Matter and Graduate School of Chinese Academy of Sciences, Fuzhou 350002, PR China

ARTICLE INFO

Article history:
Received 31 August 2010
Received in revised form
31 December 2010
Accepted 4 January 2011
Available online 13 January 2011

Keywords:
Nanostructured materials
Chemical synthesis
Electrical transport
Impedance spectroscopy
Transmission electron microscopy
X-ray diffraction

ABSTRACT

A series of $Gd_{1-x}Ca_xPO_4{\cdot}nH_2O$ nanorods were prepared using a simple hydrothermal reaction which was optimized by tuning the pH values of the precursor. The resulted nanorods were characterized by X-ray diffraction, transmission electron microscopy, Fourier transformation infrared spectroscopy, and alternative current impedance technique. It is demonstrated that all $Gd_{1-x}Ca_xPO_4{\cdot}nH_2O$ nanorods crystallized in a pure hexagonal structure. For $x = 0$, the particle dimension decreased with increasing the pH value. For $x > 0$, the solid solution limit of Ca^{2+} in $GdPO_4{\cdot}nH_2O$ nanorods was about 3 mol%, below which the lattice volume increased with increasing the doping level of Ca^{2+}. The conductivities of nanorods were highly dependent on both the particle size and Ca^{2+} concentration, as indicated by the increased conductivity as particle size reduces or Ca^{2+} doping level increases. These observations were understood in terms of the dehydration and the introduction of HPO_4^{2-} defects by Ca^{2+} doping.

1. Introduction

Nanostructured oxides have received great attention in the past decades due to the novel size- and shape-dependent properties that are fundamentally important for many potential applications [1–3]. It is believed that when the grain size falls into the nanometric range, the electrical properties will become distinct from the bulk. For instance, based on the fast diffusion of free oxygen vacancies through the grain boundaries, oxygen ion conductivity was significantly enhanced for ceria-based nanostructured solid electrolytes [4]; Similarly improved lithium-ion conductivity is also obtained for the nano-sized $LiFePO_4$ [5]. It is general that the particle size reduction is accompanied with the reduced formation energy of defects, which has resulted in a markedly increased level of nonstoichiometry for the enhanced conduction [6]. On the other hand, the surface energy for nanostructures also reduces owing to the relatively larger specific surface areas that would adsorb other species like water molecules. As a result, hydration molecules may take part in the ionic conduction, contributing to the whole conductivity of the nanocrystals at low temperatures [7–11]. One of our group's recent work confirms that surface modification by phosphate species for yttrium-stabilized zirconia yields a high proton conductivity and improved thermal stability [12]. Therefore, precise determination of the conductivities has to take into account the impacts of hydrated surface and particle sizes that are involved in the nanocrystals.

Among all nanostructured materials, rare earth phosphates are well studied for their wider applications such as luminescent or laser materials [13–18] and catalysts [19]. Significant efforts have been devoted to developing rare earth ions doped lanthanide phosphate nanoparticles, nanorods and nanowires for high selectivity and sensitivity in luminescent signals [20,21]. It should be stressed that, in addition to the excellent luminescent properties, phosphates are also known as a new class of proton conductors. For instance, CsH_2PO_4 is a typical proton conductor that exhibits a sharp increase in conductivity from 1.2×10^{-5} to 9.0×10^{-3} S/cm at the transition temperature around 230 °C [22]. It is well established that doping has a great impact on the structure and particle size which may contribute to the conductivity. A typical example is that the alkaline-earth-ions doped lanthanide phosphates with a monoclinic monazite structure has activated proton conduction at temperatures above 500 °C [23,24]. Latest work indicates that doping may play dual roles in retarding the grain growth and in creating surface defects that could contribute to the conductivity [25]. Having this mind, it is interesting to wonder what would happen for the conductivity when the alkaline earth ions are doped in lanthanide phosphate nanoparticles, since with particle size reduction, lanthanide phosphates would crystallize in a hexagonal structure [21], and since such investigations are rather rare.

* Corresponding author. Tel.: +86 591 83702122; fax: +86 591 83702122.
E-mail address: lipingli@fjirsm.ac.cn (L. Li).

0925-8388/$ – see front matter © 2011 Elsevier B.V. All rights reserved.
doi:10.1016/j.jallcom.2011.01.028

In this work, we prepared a series of Ca^{2+} doped $Gd_{1-x}Ca_xPO_4{\cdot}nH_2O$ (x = 0–0.07) nanorods by a simple hydrothermal method. The variations of conductivity with both the particle size and the concentration of Ca^{2+} were systematically studied. Based on the dehydration and introduction of HPO_4^{2-} defects, the temperature dependence of conductivities were explained for all nanorods.

2. Experimental

2.1. Sample preparation

All chemical reagents were of analytic grade and used as received without further purification. Samples with the nominal formula of $Gd_{1-x}Ca_xPO_4$ (x = 0, 0.01, 0.03, 0.05, 0.07) were prepared using a simple hydrothermal method. The preparation procedure can be briefly described as follows: Gd_2O_3 was first dissolved in diluted HNO_3 to form a given concentrated $Gd(NO_3)_3$ solution. Excess HNO_3 was removed by evaporation in fume cupboard. $Ca(NO_3)_2$ and $NH_4H_2PO_4$ were dissolved in the deionized water to form aqueous solutions. After fully mixing the solutions of $Gd(NO_3)_3$ and $Ca(NO_3)_2$ together, $NH_4H_2PO_4$ solution was added dropwisely. Then, certain amounts of NaOH solution were added to the above mixture solution to adjust the pH values to 1, 6, and 9. The resulted suspensions were poured into a Teflon-lined stainless autoclave, reacted at given temperatures for several hours, and then cooled to room temperature. The precipitates were filtered and washed thoroughly with deionized water. Eventually, the samples were dried at 80 °C in air for 3 h and milled to fine powders for further characterization.

2.2. Sample characterization

Crystal structures of the samples were determined by X-ray diffraction (XRD) using an X-ray diffractometer (Rigaku D/MAX2500) with a copper target. Si powder served as an internal standard for peak positions determination. The chemical compositions of the samples were quantitatively determined by the inductive coupled plasma optical emission spectroscopy (ICP-OES). The crystallite size, D, of the samples was estimated using the Scherrer formula: $D = 0.9\lambda/(\beta\cos\theta)$, where λ (=0.15418 nm) is the wavelength of X-ray employed, θ is the angle of diffraction peak, and β denotes the half-height width after subtracting the apparatus broadening effect. The morphologies of the samples were examined by transmission electron microscopy (TEM), which was carried out with a JEOL 2010 electron microscope working at 200 kV. The particle size distributions were obtained by counting 50–100 particles in TEM images and fitted with a Logistic peak function. The vibrational properties of the samples were measured by infrared spectra on a Perkin–Elmer Spectrum One spectrometer in the 450–4000 cm^{-1} range at a resolution of 4 cm^{-1} using a KBr pellet technique after diluting the samples in KBr. The weight ratio of the samples to KBr is set at 1%. Thermal behaviors of the samples were measured using a Netzsch STA449C thermogravimetric analyzer at a heating rate of 15 K/min in nitrogen atmosphere from room temperature to 1000 °C.

Electrical conductivities of the samples were measured by alterative current impedance technique. The powder samples were pressed uni-axially into pellets with about 7 mm in diameter and 2 mm in thickness. Silver paste was painted onto both sides of the pellets as electrodes. To obtain excellent contact between silver electrodes and pellet, the painted pellets were dried at 200 °C for 2 h before the test. Alternative current impedance spectroscopy was performed using impedance analyzer (Agilent 4294A) in the frequency range from 40 Hz to 5 MHz for a temperature range from room temperature to 150 °C with an oscillation voltage of 500 mV. All measurements were carried out in air. The impedance data were analyzed by an equivalent circuit model using the software of Zsimpwin (PerkinElmer Instruments).

3. Results and discussion

3.1. Optimum formation of $Gd_{1-x}Ca_xPO_4{\cdot}nH_2O$ nanorods

Fig. 1 shows the XRD patterns of the samples prepared at 160 °C for 12 h at different pH values. The diffraction peaks of all three samples were in good agreement with the standard diffraction data for $GdPO_4{\cdot}H_2O$ (JCPDS, Card No. 39-0232) and therefore were indexed to a pure hexagonal phase. The sample obtained at pH = 1 exhibited very sharp diffraction peaks, indicating a high crystallinity. Increasing the pH value to 6 led to the slightly broadened diffraction peaks and the increased relative intensity of line (1 0 2). Further increasing pH value to 9 greatly broadened the diffraction peaks. These observations indicate that the particle size of the samples can be tuned by tuning the pH values. The particle sizes were estimated using Scherrer formula based on the widths of two main diffraction

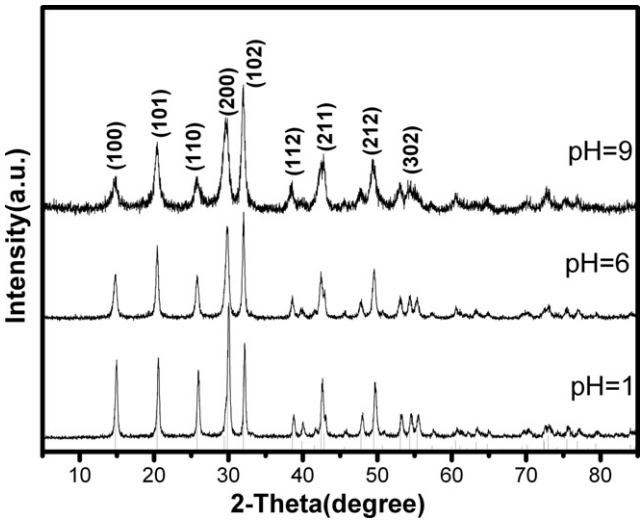

Fig. 1. XRD patterns of the samples prepared at given pH values.

lines (2 0 0) and (1 0 2). For line (1 0 2), the crystallite sizes were estimated to be 32, 25, and 17 nm, respectively, when pH value increased from 1, 6, to 9. Comparatively, based on the half height width of the diffraction line (2 0 0), the crystallite sizes were 25, 15, and 7 nm. It is obvious that the particle sizes using line (1 0 2) were all larger than those when using line (2 0 0). Therefore, the morphologies of all particles were not spherical, which is further demonstrated by TEM measurements.

Particle size and morphology of the as-prepared nanorods were examined by TEM, as shown in Fig. 2. All samples exhibited a homogeneous rod-like morphology with lengths ranging from tens up to several hundred nanometers. Here, the size distributions were obtained by counting 50–100 particles in TEM images and fitted using a Logistic peak function [46]:

$$y = \frac{4A\exp\left[-((x-x_c)/w)\right]}{\left\{1+\exp\left[-((x-x_c)/w)\right]\right\}^2} \quad (1)$$

where A specifies the peak's magnitude, x_c describes where on the X-axis the center resides, and w characterizes the peak's width. The data fit results for these parameters are listed in S3. As illustrated in Fig. 2 the average diameters of nanorods were 28, 21, and 11 nm, respectively, for the samples when prepared at pH = 1, 6, and 9. These particle sizes were nearly the same as those estimated for the line (2 0 0). A typical HRTEM image and a selected area electron diffraction (SAED) pattern for the sample obtained at pH = 1 were presented in Fig. 3. SAED pattern taken from a single nanorod indicates the single-crystalline nature. HRTEM image in Fig. 3b exhibited the clearly resolved lattice fringes. The distance between two adjacent lattice fringes was 0.605 nm, which is compatible with that of 0.598 nm for the (1 0 0) plane (JCPDS No. 39-0232). The (1 0 0) plane is parallel to the nanorod axis, which indicates that the growth direction of nanorods is along the c-axis.

From Fig. 2 it is seen that pH value of the reaction solution affects both the rod diameter and the axis ratio. Previous investigations have shown that the anisotropic growth mechanism of nanocrystals in solutions is determined by the relative chemical potentials [26,27], in which one dimensional growth is believed to occur only when the chemical potential of the monomers in solutions is much higher than the highest chemical potential of the atoms on the surfaces of nanocrystals [28]. In the present work, the nanorods obtained under weak basic condition of pH = 9 showed a lower axis ratio and smaller particle size primarily because Gd^{3+} ions are prone to precipitation as the hydroxides to reduce their

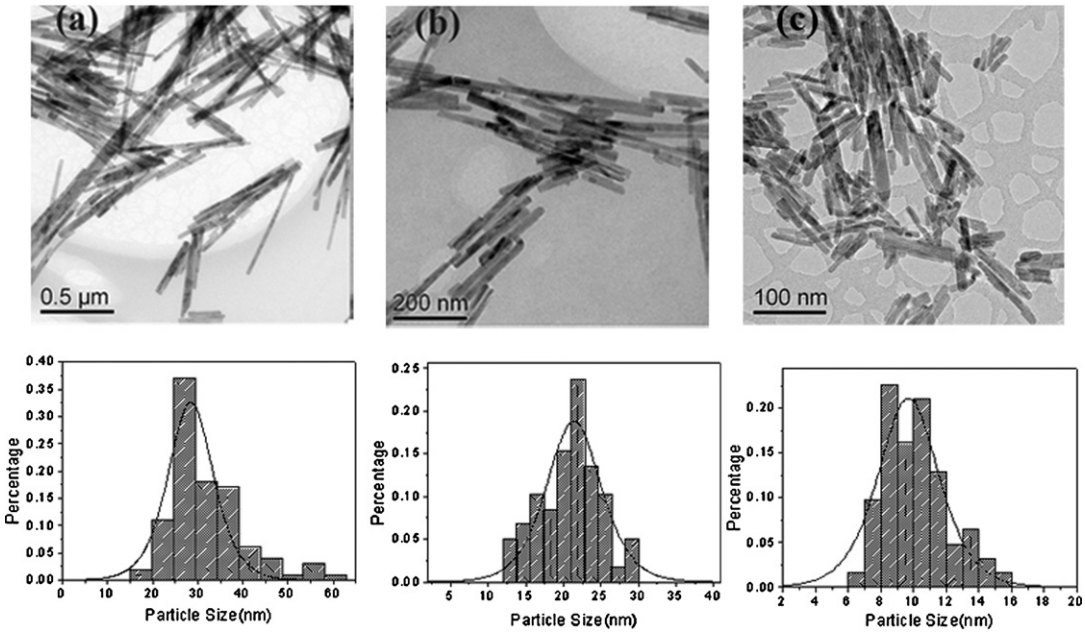

Fig. 2. TEM images of the $GdPO_4{\cdot}nH_2O$ nanorods obtained at (a) pH = 1, (b) pH = 6, and (c) pH = 9. Shown at the bottom are the corresponding rod diameter distributions.

chemical potential [29]. At acidic (pH = 1) or near neutral conditions (pH = 6) however, the precipitation of Gd^{3+} ions is suppressed, which would result in the increase in chemical potentials that promote the anisotropic growth. As a result, the nanorods obtained at pH = 1 and 6 had the higher axis ratios and larger particle sizes. Similar case has been reported by Yan et al. [29] who obtained $LaPO_4{\cdot}nH_2O$ nanorods of a high axis ratio at the presence of EDTA in the initial solution. The growth of the present nanorods along the *c*-axis can be understood from the viewpoint of the intrinsic structure of the hexagonal lanthanide phosphates: hexagonal lanthanide orthophosphate consists of the infinite linear chains that extend along the *c*-axis, and moreover the growth along the *c*-axis direction has an activation energy lower than that perpendicular to the *c*-axis [21]. Therefore, the growth rate along the *c*-axis could be much higher than others.

The influences of the reaction temperature and reaction time were also investigated with an aim to achieve the optimum condition for the formation of the $GdPO_4{\cdot}nH_2O$ nanocrystals. When the pH value was fixed at 9 and reaction time was set at 12 h, varying the reaction temperature from 100 to 170 °C did not alter the morphology and the pure hexagonal phase (S1). Instead, when the reaction temperature was set at 160 °C and pH was chosen as 9, prolonging the reaction time changed the crystallinity and grain size of the nanorods as well. As indicated in S2, when the reaction duration was fixed at 2 h, the particles size was several nanometers with a poor crystallinity. After prolonging the reaction time to 12 h, nanorods increased to several tens nanometers. Based on these observations, preparation conditions for $Gd_{1-x}Ca_xPO_4{\cdot}nH_2O$ nanorods were optimized and therefore chosen as: 160 °C for 12 h at pH = 9.

Fig. 4 shows the XRD patterns of $Gd_{1-x}Ca_xPO_4{\cdot}nH_2O$ nanorods at varied Ca^{2+} doping levels. Regardless of the doping levels, all samples crystallized in a hexagonal structure with no impurities detected. The Ca^{2+} contents were determined by ICP to be 1.4, 3.3, 5.2, and 7.4 mol% for the nominal $Gd_{1-x}Ca_xPO_4{\cdot}nH_2O$ (x = 0.01, 0.03, 0.05 and 0.07). TEM shows that Ca^{2+} doping in $GdPO_4{\cdot}nH_2O$ nanorods hardly alters the rod-like morphology and the particle dimension as indicated by TEM for x = 0.03 in Fig. 5. The impact of Ca^{2+} doping on the lattice parameter was also studied through lattice parameter calculations by Rietveld refinement

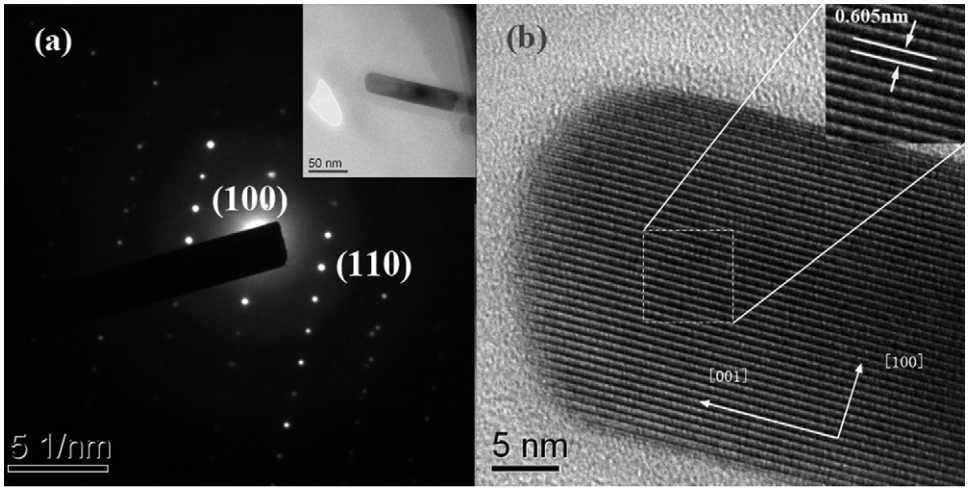

Fig. 3. (a) SAED pattern and (b) HRTEM image of a singular $GdPO_4{\cdot}nH_2O$ nanorod. Inset shows the TEM of a singular nanorod.

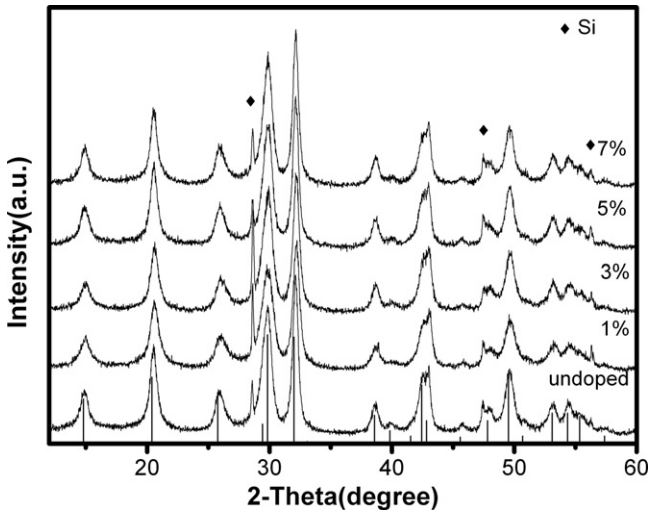

Fig. 4. XRD patterns of the Ca^{2+} doped $GdPO_4{\cdot}nH_2O$ nanorods at given doping level. Undoped sample is also shown for comparison. Symbols "♦" denote the internal standard Si.

using the Rietica program. Fig. 6 shows the relationship between the Ca^{2+} content and cell volume of $Gd_{1-x}Ca_xPO_4{\cdot}nH_2O$ nanorods. For $x = 0$, the lattice parameters were $a = 0.6924$ nm, $c = 0.6334$ nm, and $V = 0.2625\ nm^3$, which are all slightly larger than those for the bulk (JCPDS No. 39-0232). Such a lattice expansion is closely related to the small particle dimension, since the strong repulsive force arising for the surface defective dipoles may create a "negative pressures" [30]. With increasing the Ca^{2+} content, the cell volume increased, apparently in agreement with the ionic radii differences between Gd^{3+} and Ca^{2+}: the ionic radius for Gd^{3+} in 8-fold coordination is 0.105 nm, which is slightly smaller than that of 0.112 nm for Ca^{2+} with the same coordination [31]. Therefore, when larger Ca^{2+} is incorporated into the Gd^{3+} site to form the solid solutions $Gd_{1-x}Ca_xPO_4{\cdot}nH_2O$, the cell volume would increase. However, when Ca^{2+} content is larger than 3 mol%, the cell volume was kept nearly the constant within the experimental errors, demonstrating the solid solution limit of Ca^{2+} in $GdPO_4{\cdot}nH_2O$ nanorods at around 3 mol%, which is very closer to that of 4.2 mol% in the Ca^{2+} doped $LaPO_4$ [24] and 3 mol% in the Ca^{2+} doped YPO_4 [32].

3.2. Hydration termination of $Gd_{1-x}Ca_xPO_4{\cdot}nH_2O$ nanorods

Hydration termination of $Gd_{1-x}Ca_xPO_4{\cdot}nH_2O$ nanorods was examined by thermogravimetric analysis and infrared spectrum.

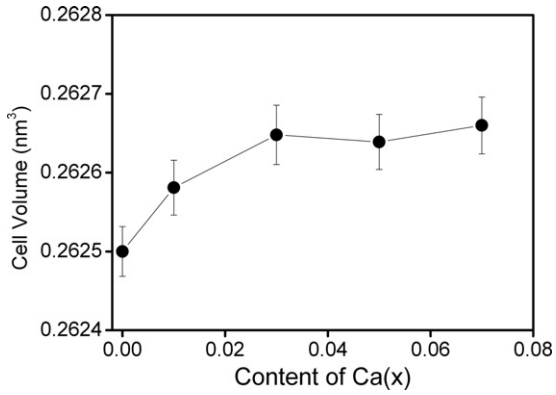

Fig. 6. Relationship between Ca^{2+} content (x) and cell volume of $Gd_{1-x}Ca_xPO_4{\cdot}nH_2O$ nanorods.

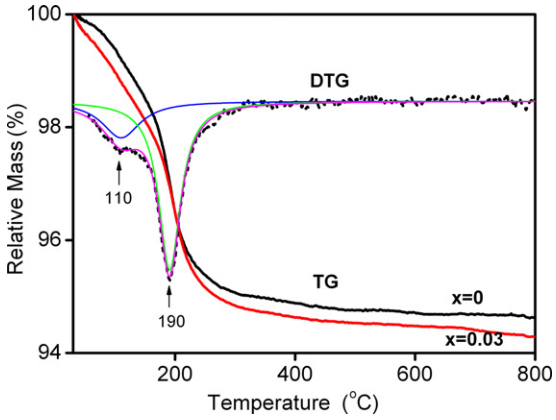

Fig. 7. TG and DTG curves of the $Gd_{1-x}Ca_xPO_4{\cdot}nH_2O$ nanorods at $x = 0$ and 0.03.

Fig. 7 shows the TG curves for nanorods $Gd_{1-x}Ca_xPO_4{\cdot}nH_2O$ at $x = 0$ and 0.03. Nanorods of other compositions exhibited the similar TG data. A continuous weight loss was observed in the temperature range from 30 to 400 °C. Derivative thermogravimetric (DTG) data for $x = 0$ (Fig. 7) clearly showed two peaks, which indicates that the mass change was composed of two processes. The first one with the DTG peak at 110 °C is corresponding to the dehydration process of surface absorbed water of the nanorods; while the second one at 190 °C is assigned to the dehydration process of water molecules from the lattice [29]. The total weight loss was 5.3 wt% for $x = 0$ and 5.6 wt% for = 0.03. It means that the water content, n, for $Gd_{1-x}Ca_xPO_4{\cdot}nH_2O$ nanorods was 0.79 and 0.83 for $x = 0$ and 0.03, slightly smaller than that of 0.97 for $x = 0.01$ or 0.91 for $x = 0.05$. All

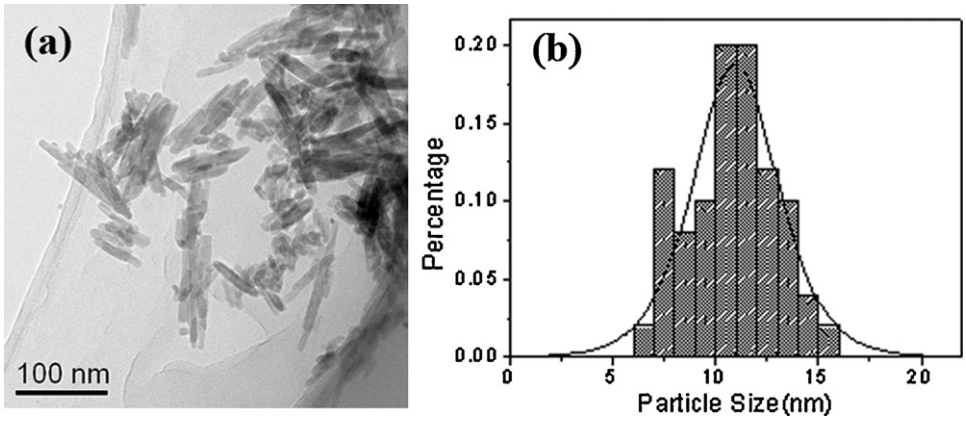

Fig. 5. (a) TEM images and (b) diameter size distributions of $Gd_{0.97}Ca_{0.03}PO_4{\cdot}nH_2O$ nanorods.

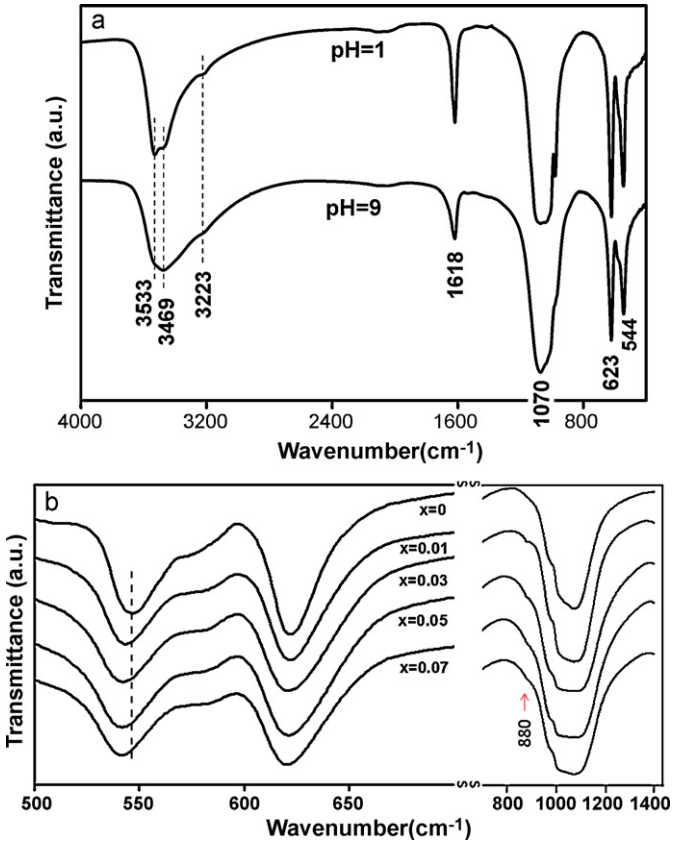

Fig. 8. (a) IR spectra for the nanorods at $x = 0$ prepared at given pH value, and (b) the enlarged vibration bands for nanorods with varied doping level x.

these water contents were consistent to those previously reported for other nanoscale systems [33].

Fig. 8a illustrates the IR spectra for the nanorods at $x = 0$ in the frequency range of 400–4000 cm^{-1}. The absorption bands observed in the range of 400–1500 cm^{-1} are attributed to the active vibrations of tetrahedral PO_4^{3-}. The infrared spectra of hydrated rare earth phosphate were widely studied [34–36]. $GdPO_4{\cdot}nH_2O$ possesses a hexagonal primitive unit cell with a space group of $P3_121(D_3^4)$ and each primitive unit cell has three molecular units, in which PO_4^{3-} anions are located at C_2 sites [35]. Site group analysis yields 5A and 4B modes, which are all IR and Raman active. Bands at 546 and 623 cm^{-1} can be assigned to A_2 modes, while the relatively broad band centered at 1070 cm^{-1} is attributed to the A_2 modes overlapped with E mode [35]. The sharp band at 1618 cm^{-1} is associated with the deformation vibration of H–O–H bonds of the water molecules [37]. The broad profile in the range 2500–4000 cm^{-1} indicates the stretching vibrations of O–H. Different from many other oxide nanoparticles in which only one broad band was observed, the broad profile for both of undoped $GdPO_4{\cdot}nH_2O$ samples consist of three bands at 3223, 3469, and 3533 cm^{-1}. The observation of the bands at 3223 and 3533 cm^{-1} confirms the existence of lattice water [38].

Ca^{2+} doping also altered the vibrational positions. As indicated in Fig. 8b with increasing the doping level from $x = 0$–0.07, vibration frequency shifted from 546 to 542 cm^{-1}. Previous investigations have shown that the vibration frequencies of the PO_4^{3-} in the rare earth orthophosphates are dependent on the ionic radius of lanthanide cations. The reduction of cation radius, such as from La to Dy, has led to a closer packing of the PO_4^{3-} group with the shortened P–O distance, which shifts the vibration bands to higher frequencies [35]. As proved by the above XRD analysis, the larger ionic radius of Ca^{2+} (0.112 nm) compared with that of Gd^{3+} (0.105 nm) led to a lattice expansion in $Gd_{1-x}Ca_xPO_4{\cdot}nH_2O$, which could reduce the packing of the PO_4^{3-} groups with the lengthened P–O distances. Therefore, with increasing the Ca^{2+} doping level from $x = 0$–0.07, the vibration bands around 540 cm^{-1} slightly shifted towards lower frequencies.

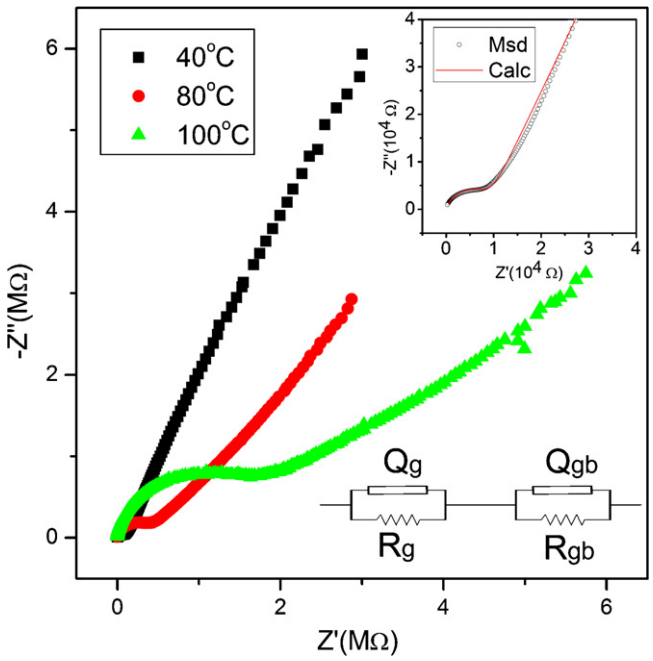

Fig. 9. Complex impendence plots for 11 nm $GdPO_4{\cdot}nH_2O$ measured at different temperatures. Inset shows the equivalent circuit model and the data fit results of the raw data measured at 40 °C.

Because of the aliovalent substitution, doping of Ca^{2+} for Gd^{3+} also introduced lattice defects. As indicated in Fig. 8b new weak absorption was observed at wave-number of 880 cm^{-1} for all Ca^{2+} doping levels. This new absorption is associated with the presence of the HPO_4^{2-} [39]. This finding is fundamentally important, since the hydrogen phosphate HPO_4^{2-} can not only compensate the charge differences between the divalent Ca^{2+} and trivalent Gd^{3+}, but also introduce the interstitial protons which would affect the conduction within the nanorods.

3.3. Conduction properties of $Gd_{1-x}Ca_xPO_4{\cdot}nH_2O$ nanorods

The conductivities of Ca^{2+} doped $GdPO_4{\cdot}nH_2O$ nanorods were determined by alternative current impedance spectroscopy, a useful technique that can distinguish the bulk conduction from the grain boundary conduction [7,40]. Typical complex impendence plots for $GdPO_4{\cdot}nH_2O$ nanorods (11 nm) at different temperatures are shown in Fig. 9. It is seen that the impedance data are composed of a semicircular arc in higher frequencies and a spike in lower frequencies, which are assigned to the grain contribution and grain boundary contribution, respectively. All impedance data were fitted by an equivalent circuit model that contains two parallel combinations of resistance R and constant phase elements Q connected in series with impedance $Z_Q = [A(jw)^n]^{-1}$, as illustrated in inset of Fig. 9, where A and n are constants for a given set of experimental data, and w is the angular frequency. The exponent, n, ranges from 0 to 1, which characterizes the constant phase elements of (RQ) subcircuits [41]. The data fit results matched well the experiment data as indicated by the solid line in inset of Fig. 9 for the raw data recorded at 40 °C. It is seen that the impedance spectra were strongly dependent on the temperature. As the temperature increased from 40 to 100 °C, the diameter for the higher frequency semicircular arc corresponding

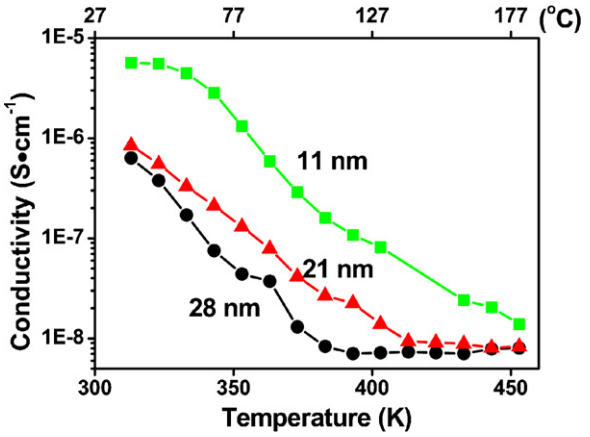

Fig. 10. Temperature dependence of conductivities for $GdPO_4{\cdot}nH_2O$ nanorods with average diameter of 11, 21, and 28 nm.

to the grain resistance also increased. Fig. 10 shows the temperature dependence of grain conductivities for $GdPO_4{\cdot}nH_2O$ nanorods with different average diameters of 11, 21, and 28 nm. Two features can be found: (1) $GdPO_4{\cdot}nH_2O$ nanorods with a diameter of 11 nm exhibited the highest grain conductivity in the whole measurement temperature range. For example, the grain conductivity for 28 nm nanorods was 4.41×10^{-8} S/cm at 80 °C. Reducing the diameter to 21 and 11 nm, the conductivity increased to 1.31×10^{-7} and 1.32×10^{-6} S/cm, respectively. (2) Regardless of the physical dimension for $GdPO_4{\cdot}nH_2O$ nanorods, the conductivities decreased with increasing the temperature, indicating a similar conduction mechanism. To explain these observations, several factors should be considered. As well known, nanoparticles usually have large surface areas which may absorb water molecules to form a hydration termination. Due to the weak bonding state, water molecules confined within the surface layers easily migrate under the external electric field to give a proton conduction [42]. It is well established that particle size reduction can enhance the surface hydration, and therefore a higher conductivity is expected. On the other hand, removal of water from the surface of nanorods during the heating process would reduce the concentration of conductive protons, which would cause a deviation from a simple thermal activation process and hence result in a nonlinear decrease of grain conductivities as temperature increases from 40 to 130 °C. As a result, the conduction in this process did not follow the Arrhenius law, and no constant activation energy could be expected [43].

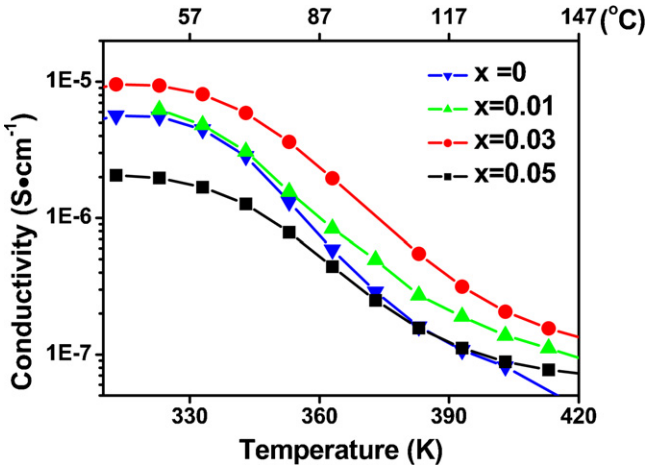

Fig. 11. Temperature dependence of conductivities for $Gd_{1-x}Ca_xPO_4{\cdot}nH_2O$ nanorods at given doping levels, x.

Temperature dependence of conductivity for Ca^{2+} doped $GdPO_4{\cdot}nH_2O$ nanorods is presented in Fig. 11. For comparison, the conductivity data for undoped $GdPO_4{\cdot}nH_2O$ with a diameter of 11 nm are also shown. For undoped nanorods, the conductivity at 90 °C was 5.88×10^{-7} S/cm. Increasing Ca^{2+} doping level to 0.03 led to a conductivity of 1.96×10^{-6} S/cm. Similar to the undoped nanorods, the grain conductivities of Ca^{2+} doped nanorods decreased with increasing temperature, showing deviation from a simple thermal activation process. Such an observation could be understood by taking into account the adsorbed water on the nanorods surface and the lattice defects. From TG analysis above, it is found that the incorporation of Ca^{2+} in $GdPO_4{\cdot}nH_2O$ lattice did not alter the water content. Therefore, hydrated surface was not responsible for the discrepancies of conductivities at different Ca^{2+} levels. The effect of lattice defects generated by Ca^{2+} doping can be a possible reason, since incorporation of Ca^{2+} generated the HPO_4^{2-} defects in nanorods, as expressed using Kroger–Vink notation:

$$CaHPO_4 \rightarrow Ca'_{Gd} + (HPO_4)^{\bullet}{}_{PO_4}$$

i.e. the effective negative charge of acceptor doping is compensated by positive defects. The presence of positive defects $(HPO_4)^{\bullet}{}_{PO_4}$ would introduce interstitial protons [44,45]. So, protonic conduction is most likely to occur via $(HPO_4)^{\bullet}{}_{PO_4}$ as the extrinsic positive defects that are necessary for the enhanced conductivity. When the Ca^{2+} doping level reached to $x = 0.05$, exceeding the solid solution limit (3 mol%) of the solid solutions, surface doping may become dominant: Ca^{2+} on the surfaces of nanorods would form the dangling bonds which may act as the surface defects. These defects may serve as the trap centers for immigrating the protons, which deteriorate the conductivity. Therefore, in comparison with other three samples, the sample at $x = 0.05$ exhibited the lowest conductivity.

4. Conclusions

$GdPO_4{\cdot}nH_2O$ nanorods with different doping levels of Ca^{2+} were prepared by a simple hydrothermal process. The solid solution limit of Ca^{2+} in $GdPO_4{\cdot}nH_2O$ nanorods was about 3 mol%. Regardless of the doping levels, all nanorods exhibited homogeneous rod-like morphologies with lengths ranging from tens up to several hundred nanometers. When the pH value of reaction solution was tuned from 1 to 9, the average diameters for undoped $GdPO_4{\cdot}nH_2O$ nanorods decreased from 28 to 11 nm. In comparison with the undoped nanorods, Ca^{2+} doping hardly altered the particle dimensions and hydrated terminations. The water content for $Gd_{1-x}Ca_xPO_4{\cdot}nH_2O$ nanorods was determined to be in the range from $n = 0.75$ to 0.97. The incorporation of Ca^{2+} into $GdPO_4{\cdot}nH_2O$ nanorods generated the HPO_4^{2-} defects, accounting for the enhanced conductivity: undoped $GdPO_4{\cdot}nH_2O$ nanorods with average diameter of 11 nm gave the highest conductivity. The variation of conductivity with temperature and Ca^{2+} concentration is closely related to the dehydration and introduction of HPO_4^{2-} defects.

Acknowledgments

This work was financially supported by NSFC under the contract (Nos. 50972143, 20903097, 20773132, 20831004), Directional program (KJCX2-YW-319), FJIRSM key program (No. SZD-08002-3), FIPYT (No. 2008F3116), and FJIRSM (No. 2010KL002).

Appendix A. Supplementary data

Supplementary data associated with this article can be found, in the online version, at doi:10.1016/j.jallcom.2011.01.028.

References

[1] Y.N. Xia, P.D. Yang, Y.G. Sun, Y.Y. Wu, B. Mayers, B. Gates, Y.D. Yin, F. Kim, Y.Q. Yan, Adv. Mater. 15 (2003) 353.
[2] G.R. Patzke, F. Krumeich, R. Nesper, Angew. Chem. Int. Ed. 41 (2002) 2446.
[3] A.P. Alivisatos, Science 271 (1996) 933.
[4] M.G. Bellino, D.G. Lamas, N.E.W. de Reca, Adv. Mater. 18 (2006) 3005.
[5] J.M. Tarascon, N. Recham, M. Armand, J.N. Chotard, P. Barpanda, W. Walker, L. Dupont, Chem. Mater. 22 (2010) 724.
[6] H.L. Tuller, Solid State Ionics 131 (2000) 143.
[7] L.J. Chen, L.P. Li, G.S. Li, J. Solid State Chem. 181 (2008) 2073.
[8] S. De, A. Dey, S.K. De, J. Phys. Chem. Solids 68 (2007) 66.
[9] S. Hara, S. Takano, M. Miyayama, J. Phys. Chem. B 108 (2004) 5634.
[10] V. Zima, M. Vlcek, L. Benes, M. Casciola, L. Massinelli, R. Palombari, Chem. Mater. 8 (1996) 2505.
[11] E. Mccaffer, V. Pravdic, A.C. Zettlemo, Trans. Faraday Soc. 66 (1970) 1720.
[12] H. Wang, X.Q. Qiu, L.P. Li, G.S. Li, Chem. Lett. 36 (2007) 1132.
[13] N. Yaiphaba, R.S. Ningthoujam, N.S. Singh, R.K. Vatsa, N.R. Singh, J. Lumin. 130 (2010) 174.
[14] C.C. Wu, K.B. Chen, C.S. Lee, T.M. Chen, B.M. Cheng, Chem. Mater. 19 (2007) 3278.
[15] Z.Y. Huo, C. Chen, D. Chu, H.H. Li, Y.D. Li, Chem. Eur. J. 13 (2007) 7708.
[16] L.X. Yu, D.C. Li, M.X. Yue, J. Yao, S.Z. Lu, Chem. Phys. 326 (2006) 478.
[17] Y.C. Kang, E.J. Kim, D.Y. Lee, H.D. Park, J. Alloys Compd. 347 (2002) 266.
[18] K. Riwotzki, H. Meyssamy, H. Schnablegger, A. Kornowski, M. Haase, Angew. Chem. Int. Ed. 40 (2001) 573.
[19] H. Onoda, H. Nariai, A. Moriwaki, H. Maki, I. Motooka, J. Mater. Chem. 12 (2002) 1754.
[20] K. Kompe, H. Borchert, J. Storz, A. Lobo, S. Adam, T. Moller, M. Haase, Angew. Chem. Int. Ed. 42 (2003) 5513.
[21] Y.P. Fang, A.W. Xu, R.Q. Song, H.X. Zhang, L.P. You, J.C. Yu, H.Q. Liu, J. Am. Chem. Soc. 125 (2003) 16025.
[22] D.A. Boysen, S.M. Haile, H.J. Liu, R.A. Secco, Chem. Mater. 15 (2003) 727.
[23] N. Kitamura, K. Amezawa, Y. Uchimoto, Y. Tomii, T. Hanada, N. Yamamoto, Solid State Ionics 177 (2006) 2369.
[24] K. Amezawa, Y. Tomii, N. Yamamoto, Solid State Ionics 176 (2005) 135.
[25] D.J. Norris, A.L. Efros, S.C. Erwin, Science 319 (2008) 1776.
[26] Z.A. Peng, X.G. Peng, J. Am. Chem. Soc. 124 (2002) 3343.
[27] Z.A. Peng, X.G. Peng, J. Am. Chem. Soc. 123 (2001) 1389.
[28] S.H. Yu, B. Liu, M.S. Mo, J.H. Huang, X.M. Liu, Y.T. Qian, Adv. Funct. Mater. 13 (2003) 639.
[29] R.X. Yan, X.M. Sun, X. Wang, Q. Peng, Y.D. Li, Chem. Eur. J. 11 (2005) 2183.
[30] L.P. Li, Y.G. Su, G.S. Li, Appl. Phys. Lett. 90 (2007), 054105.
[31] R.D. Shannon, Acta Crystallogr. Sect. A 32 (1976) 751.
[32] K. Amezawa, Y. Tomii, N. Yamamoto, Solid State Ionics 162 (2003) 175.
[33] H. Assaaoudi, A. Ennaciri, A. Rulmont, M. Harcharras, Phase Trans. 72 (2000) 1.
[34] R. Kijkowska, E. Cholewka, B. Duszak, J. Mater. Sci. 38 (2003) 223.
[35] H. Assaaoudi, A. Ennaciri, A. Rulmont, Vib. Spectrosc. 25 (2001) 81.
[36] A. Hezel, S.D. Ross, Spectrochim. Acta 22 (1966) 1949.
[37] C.C. Huang, Y.W. Lo, W.S. Kuo, J.R. Hwu, W.C. Su, D.B. Shieh, C.S. Yeh, Langmuir 24 (2008) 8309.
[38] V.V.M.V.V. Pechkovskii, L.S. Stanovaya, S.P. Suleimanov, R.Ya. Mel'nikova, L.S. Eshchenko, J. Appl. Spectrosc. 36 (1982) 631.
[39] R. Kijkowska, J. Mater. Sci. 39 (2004) 2017.
[40] E. Barsoukov, J.R. Macdonald, Impedance Spectroscopy, Wiley, NJ, 2005, p. 18.
[41] S.M. Haile, D.L. West, J. Campbell, J. Mater. Res. 13 (1998) 1576.
[42] L.J. Chen, L.P. Li, G.S. Li, Solid State Ionics 179 (2008) 712.
[43] W.B. Hu, L.P. Li, G.S. Li, J. Meng, W.M. Tong, J. Phys. Chem. C 113 (2009) 16996.
[44] N. Kitamura, K. Amezawa, Y. Tomii, T. Hanada, N. Yamamoto, T. Omata, S. Otsuka-Yao-Matsuo, J. Electrochem. Soc. 152 (2005) A658.
[45] K. Amezawa, H. Maekawa, Y. Tomii, N. Yamamoto, Solid State Ionics 145 (2001) 233.
[46] R. Brown, Pers. Eng. Instrum. News (1991) 51–54.